JUNE 1980

PPPL-1673
UC-20f



# PERFORMANCE STUDY OF THE TFTR DIAGNOSTIC NEUTRAL BEAM FOR ACTIVE CHARGE EXCHANGE MEASUREMENTS

BY

S. S. MEDLEY, R. J. GOLDSTON,
AND H. H. TOWNER

## PLASMA PHYSICS LABORATORY



## PRINCETON UNIVERSITY
## PRINCETON, NEW JERSEY

This work was supported by the U.S. Department of Energy Contract No. DE-AC02-76-CHO 3073. Reproduction, translation, publication, use and disposal, in whole or in part, by or for the United States government is permitted.

# PERFORMANCE STUDY OF THE TFTR DIAGNOSTIC NEUTRAL BEAM FOR ACTIVE CHARGE EXCHANGE MEASUREMENTS

by

S. S. Medley, R. J. Goldston, and H. H. Towner

PPPL-1673 June 1980

# PERFORMANCE STUDY OF THE TFTR DIAGNOSTIC NEUTRAL BEAM FOR ACTIVE CHARGE EXCHANGE MEASUREMENTS

by

S. S. Medley, R. J. Goldston and H. H. Towner
Plasma Physics Laboratory, Princeton University
Princeton, N. J. 08544

## ABSTRACT

A neutral beam source will be incorporated in the Tokamak Fusion Test Reactor (TFTR) charge exchange diagnostic to provide a time modulated, spatially localized enhancement of the charge exchange efflux. Two autonomous Charge Exchange Neutral Analyzer (CENA) systems are being designed for the TFTR. One system measures the plasma ion temperature along twelve vertical line-of-sight chords spaced approximately equidistantly across the torus minor diameter. The other system is dedicated primarily to measurement of ion phenomena associated with neutral beam injection heating and has a fan-like field of view along eight sight-lines in the equitorial plane. The neutral beam is steerable in order to access the viewing field of both CENA systems, though in general not simultaneously. The performance of the diagnostic neutral beam is evaluated to determine the optimal beam specifications for active charge exchange measurements. Using the optimal beam design parameters, the efficacy of the neutral doping is examined for both CENA systems over the envisioned range of the TFTR plasma density and temperature.

## 1.0 INTRODUCTION

The purpose of the Charge Exchange Neutral Analyzer (CENA) diagnostic for the Tokamak Fusion Test Reactor (TFTR) is to measure the energy distributions of both the thermal ions and the supra-thermal population arising from neutral beam injection or ion cyclotron resonance heating. These measurements yield the plasma ion temperature as well as several other plasma parameters necessary to provide an understanding of the plasma condition and the performance of auxiliary heating methods.

All diagnostics for the TFTR must meet general requirements which are significantly more demanding compared with tokamak experiments of the past. This situation arises, in part, due to the large plasma dimensions and tritium operation characterizing the TFTR device. Furthermore, the use of neutral beam injection, ion cyclotron resonance and magnetic compression heating methods either individually or in combination demands an expanded diagnostic capability. Cited below are the major functional requirements and plasma parameters relevant to the charge exchange diagnostic.

- Operating plasma parameter range

$$1 \times 10^{13} \lesssim n_e(0) \lesssim 2 \times 10^{14} \text{ cm}^{-3}$$

$$50 \lesssim a \lesssim 85 \text{ cm}$$

$$0.5 \lesssim T_i \lesssim 15 \text{ keV}$$

$$20 \lesssim E_{supra} \lesssim 200 \text{ keV}$$

- Provide ontogeny of thermal and suprathermal ion energy distributions under all heating scenarios:
  - ohmic
  - magnetic compression
  - neutral injection
  - ICRH
- Measure mass and energy resolved spectra for hydrogen, deuterium and tritium simultaneously.
- Single discharge measurement capability especially during tritium operation.
- Operate in a hostile neutron and gamma-ray environment.

The energy range for the suprathermal ions, $E_{supra}$, is a consequence of the combined neutral injection and magnetic compression heating methods. As indicated in the reference modes of operation for the TFTR device shown in Fig. 1, after ohmic startup the plasma is heated by injection of 120 keV deuterium neutral beams. During the subsequent magnetic compression phase, the beam-ion parallel energy is pumped by the order of $C^{3/2}$ where C is the compression ratio. Including the effect of additional beam energy diffusion results in ion energies approaching the quoted 200 keV. The minority ion population during strong fast-wave heating of two-ion plasmas is predicted to attain such energies as well.

To accomodate the above heating scenarios, the CENA diagnostic for the TFTR is comprised of two autonomous charge exchange analyzer systems. Each system consists of a number of identical but inde-

pendent analyzer modules. One system, shown in Fig. 2, contains 12 analyzers viewing perpendicular to the plasma along 12 colinear vertical chords spaced roughly equidistantly over the torus minor diameter. The primary function of this system is to obtain plasma ion temperature profile measurements. A second system, shown in Fig. 3, views along multiple horizontal chords in the equitorial plane. Up to 24 sightlines are available in the fan-like array, but present plans call for only 8 analyzer modules installed on selected sightlines. Although capable of thermal diagnostics, the primary function of this system is to measure the energy and pitch angle resolved distribution of the fast circulating ions associated with neutral beam heating.

A single Diagnostic Neutral Beam (DNB) is used to enable active charge exchange measurements in the viewing fields of both the perpendicular and the horizontal analyzer systems. As indicated in Fig. 3, this arrangement requires that the neutral beam be steerable in the equitorial plane. In the position perpendicular the torus centerline, the beam intersects the viewing field of the perpendicular analyzer system which is located beneath the torus. In the position tangential to the vacuum vessel centerline, the beam provides neutral doping in the field of view of the horizontal analyzer system.

Provision of a diagnostic neutral beam capability to aid in the interpretation of charge exchange measurements is of particular importance for the TFTR plasma because the operating scenarios impose potentially distorting effects, especially with regard to the thermal ion energy distribution. First, the well-known

underestimation[1] of the central ion temperature due to non-Maxwellian curvature of the charge exchange spectrum as a result of plasma radial profile effects is aggravated by the large plasma radius of the TFTR device. Second, recent theoretical studies indicate that the presence of energetic ions in the plasma due to injection of neutral beams may lead to distortion of the high energy tail of the thermal distribution.[2] With ion cyclotron resonance heating,[3] not only are energetic ion tails generated but the radial distribution of power deposition depends on experimental conditions. As a result, the ion temperature conceivably may be peaked off-axis so that passive unfolding techniques to obtain the radial temperature profile may become difficult if not impossible. The diagnostic neutral beam provides a means for identifying and interpreting such effects as noted above.

The purpose of this study is twofold:

1) To establish the neutral beam parameters, particularly the beam energy, which optimize the analyzer signal enhancement due to the neutral doping, and
2) To determine the range of TFTR plasma parameters over which the DNB is expected to provide active measurement capability.

The report presents an overview of the analysis procedure in Section 2 followed by additional detail on the steps involving the neutral beam doping code (Section 3), calculation of the charge exchange efflux (Section 4), and simulation of the charge exchange analyzer (Section 5). The effectiveness of the neutral doping as a function of plasma parameter space is investigated for the vertical (Section 6) and horizontal (Section 7) CENA systems.

The optimal beam energy is established in the course of this investigation. The question of plasma perturbation due to the DNB is examined in Section 8. Potential applications of the DNB for other than neutral doping purposes is discussed in Section 9 and Section 10 presents a summary of the study.

## 2.0 OVERVIEW OF THE ANALYSIS PROCEDURE

The approach used for evaluation of the diagnostic neutral beam performance is illustrated by the "flow schematic" given in Fig. 4. Shown is the arrangement for the horizontal CENA system (see Fig. 3) with the diagnostic beam in the tangential position and the charge exchange efflux emerging along one of the fan-like analyzer sightlines. A brief walk through the indicated factors entering the beam evaluation study provides a useful overview. Details of the various steps are presented later in the report.

The starting point is the neutral beam ion source which is characterized by the equivalent total extracted ion current at the full beam energy. In a gas cell characterized by a given neutralization efficiency part of the ion current is converted into a neutral beam which contains a mixture of atomic particles at the full, one-half, and one-third values of the extraction energy. All three energy components of the injected beam are included in the DNB analysis by specifying the full energy and total neutral beam power along with the current fractions carried by the full, half, and third energy components. The ion source model described in Appendix A was used to obtain the injected hydrogen and deuterium

neutral beam currents as a function beam energy shown in Fig. 5. A three-dimensional neutral transport code then calculates the beam attenuation for each of the energy components as the beam penetrates into the plasma. In addition to calculating the spatial distribution of the "primary" injected neutrals, the code also determines the spatial distribution of the "halo" neutrals born by charge exchange deposition of the injected beam particles. These neutral transport calculations are combined with a bounce-averaged Fokker-Planck code which calculates the slowing-down distribution of the fast circulating ions associated with Neutral Beam Injection (NBI) heating. As part of this calculation, the code also determines the radial distribution of the plasma background or "wall" neutrals. In the absence of the diagnostic beam neutrals, the Fokker-Planck code uses its calculated plasma and geometry factors to compute the charge exchange production rate for ion collisions with the wall neutrals as a function of plasma radius, and the ion energy and pitch angle. In the presence of the diagnostic beam, the Fokker-Planck code determines the additional charge exchange production due to ion collisions with the primary and halo neutrals. In both cases, the efflux attenuation of the charge exchange neutrals emerging along user specified sightlines through the plasma is calculated. The escaping neutral efflux is folded-in with the analyzer efficiency to obtain the amplitude of the measured signal. The enhancement of this signal due to the presence of the beam neutrals is the criterion for the efficacy of the DNB doping.

For the analysis of the vertical CENA system the same procedure is used except the DNB injects normal to the plasma

centerline and the charge exchange efflux is calculated along vertical chords distributed across the plasma minor diameter. In this analysis the Fokker-Planck code was used mainly to calculate charge exchange production associated with the thermal ions, though the charge exchange flux from the slowing-down beam ions may be treated as well.

Both the neutral transport and Fokker-Planck codes require input of the radial profiles for the ion and electron temperatures and the electron density as well as several other plasma and TFTR machine parameters. The reference temperature and density profiles[4] used in this study are shown in Fig. 6. Radial profiles of the density and energy of the wall neutrals given in Fig. 7 were also generated by the BALDUR transport code.[5] These profiles are used only for comparison with similar profiles produced by the analysis codes in this study and not as input conditions. The other plasma and machine parameters used in the performance analysis are listed in Appendix B and will be referred to in this report, along with the temperature and density profiles of Fig. 6, as the "reference parameter set."

## 3.0 NEUTRAL BEAM DOPING

A description of the salient features of the 3-dimensional neutral transport code used to model the DNB doping is presented in this section. Another report providing a more complete account of the code is in preparation.[6]

The neutral transport code, NBDEN, accepts as input data the following information. The direction of the diagnostic neutral

beam in the equitorial plane of the torus is specified by the toroidal location and length of the major radius perpendicular to the tangent point of beam center trajectory. The beam itself is characterized by the ion source extraction energy, the total neutral beam power, and the current fractions of the full, one-half, and one third atomic neutral components. The cross section of the beam is partitioned into a two-dimensional grid of beamlets which are weighted according to a bi-Gaussian distribution to model the beam current profile.

The three-dimensional capability of the code is achieved by toroidal, elevational, and radial partitioning of the plasma into spatial bins nested around the plasma centerline. Up-down symmetry of a circular or non-circular minor plasma cross section around the equitorial plane is assumed and transport is calculated on only the top half plane. In this study, the number of partitioning bins is fixed but the bin "density" can be varied for statistical purposes by restricting the partitioning region to any toroidal angular segment.

The code accepts as input plasma parameters steady state radial profiles of the electron density and the electron and ion temperatures. Other plasma parameters specified are: major radius, minor radius (vertical and horizontal), plasma atomic number and $Z_{eff}$, impurity atomic number and mass, and the direction of the plasma current. Values for these parameters used in this study are given in Appendix B. Variation of the plasma density and temperature is effected by scaling the profiles given in Fig. 6 by a multiplicative factor. This procedure avoids any significant change in the profile shape which simplifies interpretation of the results.

The neutral transport is advanced by analytic calculation of the exponential attenuation, $e^{-\beta_n}$, of neutral density of the three beam energy components. The exponent, $\beta_n = \int_0^L n_e(\rho)\sigma_T^n(E,\ell)d\ell$, is evaluated locally along the beam trajectory using the input plasma parameters. Here $\sigma_T$ is the total cross section for deposition of the neutrals due to charge exchange collisions with plasma ions and impurities, and ionizing collisions with electrons, ions and impurities. The analytic expressions used for the various cross sections are given in Appendix C.

In the deposition of an injected beam particle, designated as a primary neutral, by a charge exchange collision with a plasma ion, the plasma ion becomes a neutral which is referred to as a halo neutral. Using the Monte Carlo technique, the code tracks the halo neutral through multigeneration charge exchange events until the final event is either an ionizing collision or the particle is lost from the plasma region. As will be evidenced later in the report, the halo neutrals can significantly contribute to, or even dominate, the doping effect of the diagnostic beam for active charge exchange measurements. This arises, in part, due to the fact that the halo neutrals have an energy distribution characterized by the plasma ion temperature. The charge exchange production rate in the halo energy regime often exceeds the corresponding rate at the primary neutral energy by an order of magnitude or more, as will be demonstrated shortly.

As a final remark concerning the transport code, the densities of the deposited ions, surviving primary neutrals, and created halo neutrals are registered in the appropriate spatial bins

described above. These density distributions are then available either for a variety of graphics displays or for subsequent use in the code discussed in the next section which computes the contribution of the doping neutrals to the charge exchange production rate. Before proceeding to this section, however, some examples of the transport code graphic displays are presented to illustrate the salient features of the diagnostic beam doping properties.

Application of the DNB doping for the vertical CENA system is illustrated in Fig. 8. Plot (A) is a top view of the torus showing the DNB path normal to the plasma centerline at a toroidal position crossing the vertical CENA sightlines (not shown). The primary and halo neutral densities as a function of plasma penetration length along the DNB trajectory are displayed respectively in plots B and C. The broken curve in these plots gives the minor radius (right hand ordinate) corresponding to position along the beam penetration length. For this case an 80 keV neutral deuterium beam was used with current fractions as given in Fig. 5. Of note is the good primary neutral penetration and a similarly shaped halo distribution having a density roughly 60% of the primary density. Plot D shows the ion deposition profiles as a function of plasma minor radius for the full, half, and third energy components of the diagnostic beam. Plot E is best visualized as a top view of the beam corresponding to plot A showing contours of the halo neutral density as a function of major radius (ordinate) and toroidal angle (abscissa). This illustrates, as anticipated, that the halo neutrals diffuse to form a spatially extended shroud around

the primary beam. The halo neutrals therefore affect not only the doping aspect of the DNB, but the effective spatial resolution as well. The equivalent temperature of the halo neutrals as a function of plasma minor radius is presented in plot F, illustrating the earlier remark that the halo neutral energy is characterized by the plasma ion temperature.

Use of the DNB doping for the horizontal CENA system (see Fig. 3) is illustrated in the next series of plots for the case of an 80 keV hydrogen neutral beam. Fig. 9 presents plots of the primary neutral density. The configuration of the DNB trajectory and five horizontal CENA sightlines are shown in plot A. The direction of the plasma current, $I_p$, as indicated is counter-clockwise throughout this report. Plots B-F are associated with the analyzer sightlines as noted at the top. The abscissa corresponds to the distance along the relevant analyzer sightline with zero being the outer edge of the plasma. The solid curves, therefore, give the profile of the primary neutral density as a function of position along the analyzer sightlines. The arrangement of Fig. 10 is identical, except the solid curves show the density of the halo neutrals. In comparing Figs. 9 and 10, several features are of note. First, the variation in width of the primary neutral plots simply reflects the oblique viewing angle across the beam. The relatively broader halo density profiles, however, evidence the spatial diffusion of the halo particles. The raggedness of these profiles stems from statistics of the Monte Carlo treatment used for the halo calculation.

Figure 11 shows the primary and halo neutral density as a function of distance along the beam axis. As in the previous example (see Fig. 8), the two neutral distributions have similar shapes but the halo density has decreased to around 25% of the primary density. This is explicable in terms of collision cross sections, since for 80 keV-H° the ratio of ionizing to charge exchange collisions is greater than for 80 keV-D° which leads to proportionately fewer charge exchange collisions and hence a reduction in halo neutral creation.

To provide a DNB doping data base for this study, the calculations described above were carried out using hydrogen and deuterium neutral beams for both the vertical and horizontal CENA systems. For each beam species, beam energies of 20, 40, 60, 80, and 100 keV were examined using the full, half, and third energy current fractions provided by Fig. 5.

## 4.0 CHARGE EXCHANGE SPECTRUM

In this study, the energy distribution of the charge exchange neutrals entering the CENA analyzer systems is simulated using the BAFPS code[7] which advances in time a numerical solution of the bounce-averaged Fokker-Planck equation describing the slowing-down energy distribution of Neutral Beam Injected (NBI) heating particles. While a detailed description of the code is beyond the scope of this report, a brief review of the code methodology is given below to facilitate an understanding of the results to be presented later in this paper.

The BAFPS code accepts as input data the plasma/machine parameters listed in Appendix B and radial profiles of the electron

density, electron temperature and ion temperature (see Fig. 6). Certain input data and collision cross sections (see Appendix C) are used to calculate the "wall" neutral density profile[8] and to estimate the radial energy distribution of these neutrals. In this routine, the plasma edge neutral density and temperature were adjusted to optimize agreement between the BAFPS code density profile and the Monte Carlo generated reference profile obtained from the BALDUR code as shown in Fig. 7. Good agreement is obtained over the plasma region ($r/a \lesssim 0.9$) using $n_o(a) = 3.5 \times 10^8$ cm$^{-3}$ and $T_o(a) = 35$ eV as evidenced by the profile comparison shown in Fig. 12. These edge parameters remained fixed throughout the study.

The deposition of the NBI heating particles as a function of plasma radius, beam energy, and pitch angle is accomplished essentially in the same manner as described earlier (Section 3.0) for attenuation of the DNB particles in the neutral transport code. The time evolution of the initial energy distribution so obtained for each beam energy component is advanced by the BAFPS code as the beam particles collisionally "slow down" and heat the plasma electron and ion populations. Included in the code are the effects on the ion slowing-down distribution of drag, energy diffusion on ions and electrons, and pitch angle scattering on plasma ions and impurities. A simplified orbit-loss estimate for counter-injected beam ions and charge exchange losses are treated. However, the input plasma conditions are not advanced in time due to the presence of NBI heating. This caveat while obviously limiting the code applications, on the other hand enables turnaround calculation of effects which are essential to eval-

vation of the DNB doping performance.

As the calculation of the fast-ion energy distribution proceeds, the code accumulates (at designated time steps) the charge exchange spectrum observed along sightlines through the plasma which are specified by the user. This is accomplished by segmenting the sightline and multiplying the locally determined ion energy distribution by the corresponding locally calculated "efflux propagator." This propagator is the product of the charge exchange production rate and the attenuation factor for neutral escape along the sightline. Both terms, of course, are energy dependent. The appropriate relative energy, $E_{rel}$, for the charge exchange interaction is given by:

$$E_{rel} = \frac{E_o}{A_o} + \frac{E_p}{A_p} - 2\cos\theta\left[\frac{E_o}{A_o} \cdot \frac{E_p}{A_p}\right]^{1/2} \qquad (1)$$

where $E_o$, $A_o$ are the incident neutral energy and mass, respectively, and $E_p$, $A_p$ are the corresponding quantities for the plasma ion. Here $\theta$ is the enclosed angle between the ion and neutral velocity vectors and $E_{rel}$ is in units of energy per AMU. Since the pitch angle of the candidate plasma ion must lie within the analyzer acceptance cone centered on the sightline, in effect $\theta$ is the angle enclosed by the neutral beam axis and the anlayzer sightline. The charge exchange production rates on the "wall" neutrals as well as he DNB primary and halo neutrals, if present, are thus calculated in the conventional manner once the appropriate value for $E_{rel}$ is known. For the isotropic plasma-wall and beam-halo neutrals, $E_o = 3/2\ T_o$, is the corresponding neutral energy

and $\theta = 90°$. For the DNB primary neutrals, $E_o$ is determined by the energy components of the beam and the $\theta$ depends on the angle set between the beam axis and the analyzer sightline. The attenuation factor in the efflux propagator is determined along the sightline escape path using the same procedure as for the attenuation of the injected NBI and DNB neutrals (see Section 3.0).

To recapitulate briefly, the bounce-averaged Fokker-Planck code calculates:

1) the slowing down energy distribution of neutral heating beam ions (including the plasma thermal ion distribution), and

2) the local production and attenuation of charge exchange neutrals along specified sightlines through the plasma. In combination with the neutral transport code, the contribution of the plasma-wall, DNB-primary, and DNB-halo neutrals to the observed charge exchange efflux can be calculated, individually or collectively.

## 5.0 ANALYZER MODEL

The vertical (Fig. 2) and horizontal (Fig. 3) CENA systems together contain up to twenty modular analyzers which use a semi-circular region of parallel electric and magnetic fields to accomplish mass and energy resolution, respectively. A cross sectional schematic showing plan (lower) and elevation (upper) views of the prototype E||B analyzer under construction at PPPL is given in Fig. 13. Specifications for the major components of the analyzer are contained in Appendix D along with certain parameters of the vacuum interface between the analyzer and the torus vacuum vessel.

As shown in a previously reported Monte-Carlo ion trajectory analysis which included magnetic and electric fringe field effects,[9] ions of different charge-to-mass ratio, e/M, form linear mass columns at the detector plane with displacement of the species parallel to the electric field, $\mathcal{E}$, given by

$$x_j = \frac{\pi^2}{2} \frac{\mathcal{E}}{B^2} \left(\frac{M}{e}\right)_j \quad . \tag{2}$$

Under the action of the magnetic field, B, singly charged ions of energy, E, are dispersed along the associated mass columns according to

$$Y_j = \frac{2\sqrt{2}}{eB} \sqrt{ME} \quad . \tag{3}$$

The detector is a large area microchannel plate configured with three mass columns to measure $H^+$, $D^+$ and $T^+$, simultaneously. Each *mass column is partitioned into 75 detector elements of width* $\Delta Y$. The energy resolution follows directly from Eq. 3:

$$\frac{\Delta E}{E} = \frac{eB}{\sqrt{2}} \frac{\Delta Y}{\sqrt{ME}} \quad . \tag{4}$$

Units are MKS.

The instrumental response function for the analyzer is the subject of a separate study now in progress in which earlier analytic and Monte-Carlo methods[10] have been expanded to include effects such as: 1) analyzer electric and magnetic fringe fields, 2) scattering losses, and 3) particle loss due to reionization in

the flight tube connecting the analyzer to the torus. In calculating the reionization loss, use is made of a vacuum analysis[11] of the vertical and horizontal CENA systems which calculates pressure distributions in the flight tube resulting from gas loads in both the analyzer and the torus. Details of the analyzer response study will be reported at a later date. The computer evaluated response functions used in this report are exhibited in Fig. 14 for the vertical (upper plot) and horizontal (lower plot) CENA analyzers. These curves represent the effects of: 1) the analyzer acceptance geometry, 2) flight tube reionization losses, 3) stripping cell efficiency and scattering losses, 4) the energy window, $\Delta E$, of the detector including variation with detector anode position, and 5) the detector sensitivity.

At this point, it is convenient to establish the criterion used to gauge the efficacy of the DNB doping. The bounce-averaged Fokker-Planck code calculates the line-integrated charge exchange efflux [particles/(sec·cm$^2$·steradian·eV)] both with and without the contribution due to the diagnostic beam neutrals. The spectrum without the DNB contribution is subtracted from that with the DNB. This difference is multiplied by the analyzer response [cm$^2$·steradian·eV] to yield detector signal enhancement [particles/sec] due to the presence of the diagnostic beam neutrals. For each analyzer sightline through the plasma, the average signal enhancement in the energy window, $\Delta E$, of a detector element is determined and the resulting averages are summed over all detector elements within a specified energy range to obtain the "total detector signal enhancement." For the thermal spectra, the energy range

was typically 2-10 $kT_i$. For the fast ion slowing-down distribution of injected 120 keV-D° beams, the energy range was chosen to be 20-140 keV. Maximization of the "total detector signal enhancement" is the criterion for best performance of the DNB doping.

A rough criterion for the minimum useful signal enhancement due to DNB neutrals is obtained in the following way. Let $\dot{N}_p$ be the total detector signal count rate due to charge exchange on the plasma (or wall) neutrals. In a measurement time interval, $\Delta t$, the statistical fluctuation in the count is $(\dot{N}_p\,\Delta t)^{1/2}$. For the total count rate due to the plasma plus the DNB neutrals, $\dot{N}_B$, the corresponding fluctuation is $[(\dot{N}_p + \dot{N}_B)\Delta t]^{1/2}$. The fractional uncertainty the count rate due to the DNB neutrals alone is then

$$\frac{\Delta\dot{N}_B}{\dot{N}_B} = \frac{[(2\dot{N}_p + \dot{N}_B)\Delta t]^{1/2}}{\dot{N}_B\,\Delta t} \quad . \tag{5}$$

Putting $\zeta = \left(\frac{\Delta\dot{N}_B}{\dot{N}_B}\right)^2 \Delta t$, Eq. 5 can be expressed as a quadratic in $\dot{N}_B$:

$$\zeta\dot{N}_B^{\,2} - \dot{N}_B - 2\dot{N}_p = 0 \quad . \tag{6}$$

Solution of Eq. 6 for desired values of $\Delta\dot{N}_B/\dot{N}_B$ and $\Delta t$, and a given $\dot{N}_p$ then yields the minimum useful "total detector signal enhancement," $\dot{N}_B$.

## 6.0 VERTICAL CENA ANALYSIS

The analysis of the vertical CENA system shown in Fig. 2 will be illustrated for an 80 keV deuterium beam. For this case, the primary and halo neutral densities as a function of beam penetration

length are given in plots (b) and (c), respectively, of Fig. 8. The sightlines were chosen to intersect the equitorial plane at minor radii of 0, 15, 30, 45, and 55 cm as shown in Fig. 15. The reference plasma profiles (Fig. 6) and plasma parameters (Appendix B) are used in the BAFPS code (*no* NBI heating) to calculate the thermal charge exchange neutral efflux spectrum shown in Fig. 16 both without (BEAM OFF) and with (BEAM ON) the DNB doping. Also shown is the difference spectrum due to charge exchange only on the DNB neutrals (BEAM ON - BEAM OFF) and the efflux ratio. In the last plot, the asterisks denote the lower and upper limits of the energy range spanned by the detector. As is evident, the efflux ratio is significantly greater than unity over the energy range of 2-10 kTi (10-50 keV) and varies both with energy and analyzer sightline radius. The product of the efflux and analyzer response (Fig. 14A) yields the analyzer signal spectra shown in Fig. 17 corresponding to each neutral efflux spectrum of Fig. 16. This analysis was carried out for diagnostic beam (full) energies of 20, 40, 60, 80, and 100 keV for both hydrogen and deuterium neutrals using the reference plasma profiles/parameters noted above and the fractional energy neutral currents given in Fig. 5. Following the precedure described in Section 5.0, the "total detector signal enhancement" is obtained for each sightline in the energy range 2-10 kTi using the results of Fig. 17c associated with each run. The total detector signal enhancement as a function of the beam full energy is shown in Fig. 18 for the two neutral species. The DNB doping efficacy at a given beam energy is greater for deuterium than for hydrogen. Although the

efficacy is monotonically increasing over the chosen energy range, a maximum beam energy of 80 keV is adopted as a reasonable compromise between good efficacy and proven ion source technology. In the remainder of this section, the analysis is performed using an 80 keV deuterium beam which will be referred to as the reference DNB for the vertical CENA system. The dependence of the reference DNB efficacy on plasma parameters is examined as well as some characteristics of the neutral doping.

Variation of the doping efficacy with plasma parameters was accomplished by scaling the electron density and/or temperature (Te = Ti) profiles shown in Fig. 6 with a multiplicative factor. In Fig. 19, the variation of the total detector signal enhancement with temperature is displayed for a fixed electron density of $n_e(o) = 5 \times 10^{13}$ cm$^{-3}$. The central density of the wall and beam primary/halo neutrals as a function of temperature is shown in Fig. 20. Clearly, the roughly two order of magnitude increase in diagnostic beam induced signal seen in Fig. 19 cannot be accounted for by the modest variation in density of the beam neutrals with temperature. To explain this situation, first consider Fig. 21 which shows the ratio of beam to wall induced charge exchange efflux for two 80 keV-D° cases: 1) efflux enhancement ratio due to the combined effects of primary and halo neutrals (top), and 2) efflux ratio due to only primary neutrals (bottom), the halo component being excluded. Denoting the combined ratio by $(S_p + S_H)/S_w$ and the primary only ratio by $S_p/S_w$, one can determine the halo contribution relative to that of the primary by

$$\frac{[(S_p + S_H)/S_W - S_p/S_W]}{S_p/S_W} .$$

Furthermore, as seen from Fig. 8, the primary neutral density, $n_p$, is close to double the halo density, $n_H$. Normalizing the relative primary and halo contributions to unit density provides the following factor which characterizes the doping effectiveness of halo neutrals relative to primary neutrals

$$K = \frac{n_p}{n_H} \frac{[(S_p + S_H)/S_W - S_p/S_W]}{S_p/S_W} \quad . \qquad (7)$$

Using Fig. 21 to calculate a few representative values, it is seen that $K \cong 1.5\text{-}4.5$ with larger values corresponding to higher fast neutral energies. This supports an earlier claim that the halo neutrals can contribute significantly to the effectiveness of beam doping for the measurement of $T_i$ by charge exchange in large tokamaks.[12] By way of explaining the halo neutral effectiveness, it is recalled that energy of the halo neutrals reflects the local mean ion energy, $E_o \cong 3/2\ kT_i$. For the parameters pertaining to the example under discussion ($E_o$ = 7.5 keV, $E_B$ = 80 keV, $A_o$ = $A_B$ = 2) it can be seen from Eq. (1) that the relative energy for charge exchange on the halo neutral is $E^H_{rel} \sim 7.5$ keV [$E_p/2 \sim 7.5$ and $\theta = 0°$] while for the 80 keV-D° primary $E^p_{rel} \sim 44$ keV. The ratio of the corresponding charge exchange production rates is $\langle\sigma v\rangle_H/\langle\sigma v\rangle_p \cong 2.5$ in agreement with the value of K deduced above using Eq. (7).

Returning to the earlier discussion concerning Fig. 19, it can be stated that the halo neutrals dominate the observed beam doping. The sharp initial rise of the enhancement is due to decreasing efflux attenuation with increasing energy and the subsequent roll-off

is due to the combined effects of a modest drop in halo density along with a roll-over in the halo charge exchange cross section due to coupling of the halo energy and the local ion temperature.

An important factor in the DNB application is the range of electron density over which the doping facilitates measurement of the central ion temperature. Using fixed reference plasma parameters and temperature ($T_e(0) = T_i(0) = 5$ keV) profiles, the electron density profile of Fig. 6 was scaled by multiplicative factors to generate the results shown in Fig. 22. As before, an 80 keV deuterium doping beam was used but in this case the total detector signal enhancement was determined over an energy range of 5-10 $kT_i$ in order to discriminate against the signal enhancement from the lower temperature off-axis region of the plasma. With increasing electron density, the signal enhancement drops rapidly as can be seen from Fig. 22. This effect is due in part to increasing attenuation of the incoming doping beam neutrals (see Fig. 23) and stronger attenuation of the emerging charge exchange efflux. The situation at high electron densities is not improved by the use of a more penetrating hydrogen beam at the same energy because the attendant reduction in both neutral current (see Fig. 5) as well as charge exchange production rate due to elevated interaction energy results in less signal enhancement than obtained using a deuterium beam.

An estimate of the electron density cut-off for useful DNB doping measurement of the central ion temperature is obtained using the criterion established by Eq. (6). Adopting a DNB count rate uncertainty of $\Delta\dot{N}_B/\dot{N}_B = 0.1$, a measurement time resolution of

$\Delta t$ = 20 msec, and a code calculated background total count rate of $\dot{N}_p = 5\times10^3$ particles/sec, the solution of the quadratic yields a required beam induced count rate of $\dot{N}_B = 5 \times 10^3$ particles/sec. Inspection of Fig. 22 reveals that these count rates correspond to a density cut-off of $n_e(0) \cong 1.2 \times 10^{14}$ cm$^{-3}$. Although this value falls short of the $n_e(0) = 2.0 \times 10^{14}$ cm$^{-3}$ upper operating density for the TFTR, it is necessary to point out that the above calculation represents a full bore (a = 85 cm) plasma discharge. In practice, maximum TFTR density operation is achieved during the magnetic compression scenario which reduces the plasma minor radius to a $\cong$ 55 cm. To obtain a more realistic doping cut-off density, the above value should be scaled by the ratio of the uncompressed-to-compressed minor radii. This leads to an operational cut-off density of $n_e(0)_C \cong 1.8 \times 10^{14}$ cm$^{-3}$ which is within 10% of the envisioned upper density limit for the TFTR. Although this density cut-off applies for a 5 keV central plasma temperature, it is in fact very conservative since low count rates only from particles in the 5-10 $kT_i$ Maxwellian tail were used. For a full bore $T_i$ = 1 keV plasma, the density cut-off for DNB doping is $n_e(o) \sim 3\times10^{13}$ cm$^{-3}$ using the same criteria.

## 7.0 HORIZONTAL CENA ANALYSIS

The analysis of the horizontal CENA system shown in Fig. 3 will be illustrated using an 80 keV hydrogen doping beam. For this case, the primary and halo neutral density characteristics are given in Figs. 9-11. The beam aiming and chosen analyzer sightlines are illustrated in Fig. 24. As shown on the figure, the major radius of the beam tangency is 265 cm. For the selected analyzers, the

corresponding tangency radii (not shown) are 300, 260, 210, 140 and 40 cm in order of the assigned sightline number 1-5. In the same ordering, the major radii of the intersection between the beam axis and the analyzer sightlines are 304,272,265,270, and 285 cm.

The bounce-averaged Fokker-Planck code was used to calculate the charge exchange efflux spectra associated with the slowing-down distribution for co-injected heating beams in the TFTR using the NBI simulation parameters listed in Appendix B. Note that in the following sequence of figures illustrating typical analysis output, each efflux curve is identified with an analyzer sightline in accordance with a keyed line-style as depicted in Fig. 24. Shown in Fig. 25 is the charge exchange spectra along each of the five analyzer sightlines both in the absence (BEAM OFF) and in the presence (BEAM ON) of the DNB doping neutrals. The BEAM ON case includes the doping contributions of both the primary and halo neutrals. The familiar full, half, and third energy peaks in the slowing-down energy distribution of the 120 keV deuterium heating beam particles are evident. Although it can be seen that the DNB preferentially enhances the charge exchange efflux at higher energies, this effect is better exhibited by the plots shown in Fig. 26. Here the top plot shows the difference between the efflux spectra with and without the DNB doping (BEAM ON - BEAM OFF); that is, the efflux due to charge exchange interactions on only doping neutrals. The lower plot shows the ratio (BEAM-ON/BEAM OFF) of the efflux spectra given in Fig. 25. When the halo neutrals are excluded from the analysis, the efflux difference and ratio spectra given in Fig. 26 are reduced by less than ~10%, showing that the primary neutrals dominate the enhancement of the charge exchange efflux for

the horizontal CENA doping application. As noted earlier, just the opposite result occurs for the vertical CENA doping case. Explanation of this behavior follows directly from Eq. (1). Because of the acute angle of intersection between the diagnostic beam axis and a given analyzer sightline, the relative energy for the charge exchange reaction is significantly lower for the primary beam neutrals than for the isotropic halo neutrals even though the energy of the primary neutrals greatly exceeds that of the halos. The reduction of the beam-on/beam-off ratio as the beam-sightline intersection angle increases stems from a combination of the above effect and the drop in primary neutral density due to the attendantly larger DNB penetration length. The density of wall neutrals and the primary/halo beam neutral components as a function of penetration distance measured along the beam axis is shown in Fig. 29. The positions of the sightline intersections with the beam are flaged according to the sightline numbers (see Fig. 24).

The analyzer response shown in Fig. 14B is applied to the preceeding efflux spectra to obtain the curves for the analyzer signal as a function of fast neutral energy shown in Fig. 27. The asterisks on these plots denote the lower and upper limits of the energy range spanned by the detector at a fixed analyzer magnetic field of B = 3.4 kGauss. In order of increasing sightline number (see Fig. 24), the acute intersection angles between the beam axis and the analyzer sightlines are 24, 31, 39, 49, and 61 degrees. For a time resolution of $\Delta t$ = 10 msec, the nominal detector count rate threshold for useable signal levels is $\sim 10^3$ cps. Thus from Fig. 27C it can be seen that DNB doping measurements under the

conditions of this example are feasible for all analyzer sightlines whose intersection angle does not exceed ~50°. Consequently, for this case localized DNB doping measurements of the fast-ion slowing-down distribution over a wide range of particle energy and pitch angle scattering are feasible simultaneously along multiple sightlines due to the design of the horizontal CENA and DNB doping arrangement. The influence of diagnostic beam energy and plasma parameters on the DNB doping efficacy for the horizontal CENA system is considered next.

As before, to obtain a parameter characterizing the efficacy of the beam doping, the beam induced signal increase exemplified in Fig. 27C is summed over all detector elements within a specified energy range to determine the total detector signal enhancement. In the present application, a low energy limit of 20 keV was chosen in order to include the third energy component of the injected 120 keV deuterium neutrals and a high energy limit of 140 keV to encompass energy diffusion of the captured particles. The calculations described above were carried out under the same plasma/NBI conditions with DNB energies of 20, 40, 60, 80, and 100 keV using both hydrogen and deuterium doping species. Shown in Fig. 28 is the resulting total detector signal enhancement as a function of diagnostic beam extraction energy for the two neutral species. Each curve corresponds to an analyzer sightline having the same line-style legend as given in Fig. 24. With increasing beam energy, the doping efficacy increases strongly up to energies in the 60-80 keV range and less rapidly for higher beam energies. A nominal beam energy of 80 keV is again chosen as a reasonable compromise between

good doping efficacy and proven ion source technology. On the basis of Fig. 28, both deuterium and hydrogen beams have comparable effectiveness. However, a hydrogen beam has the following forseeable advantages over a deuterium beam: 1) better penetration at higher plasma electron densities, 2) less sensitivity of doping effects to variations in the actual operating energy (see Fig. 28) of the DNB ion source, and 3) no beam-plasma neutron production which conceivably might introduce a perturbation to the neutron diagnostics viewing the DNB region. In view of the above considerations, an 80 keV hydrogen neutral beam is adopted as the reference for the horizontal CENA system.

For measurement of the fast ion slowing-down spectra with the horizontal CENA system, characterizing the scaling of the signal enhancement with variations in the density and temperature of the plasma is a somewhat complicated matter. This arises because the plasma temperature and density influence both the spatial deposition of the NBI particles as well as the evolution of the slowing down energy distribution. Furthermore, in practice the NBI injection angle will change with different electron density regimes in order to optimize the heating efficiency, thus introducing yet another parameter. For the purposes of this report, therefore, the effect of plasma parameter variation on DNB doping efficiency will be confined to some general observations.

First, the plasma ion and electron temperature has only a modest effect on the primary neutral density in the range $T \geq 1\text{-}10$ keV relevant to the TFTR. This occurs because the collision energy is dominated by the beam neutral energy. Thus the

variation in primary neutral density with plasma temperature for the 80 keV hydrogen beam is expected to be comparable to that exhibited for the 80 keV deuterium beam in Fig. 20. Second, since the primary neutral component of the doping density dominates the enhancement of the fast neutral spectra, an increase in electron density will reduce the primary density (and hence signal enhancement) roughly exponentially as determined by the beam attenuation, $e^{-\beta n}$ as discussed earlier in Section 3.0. As a rough guide, it can be seen from Fig. 29 that the primary attenuation over the most useful portion of the beam penetration distance (~ , is approximately $e^{-\beta n} \simeq 10^{-1}$ for $n_e(0) = 5 \times 10^{13}$ cm$^{-3}$. Thus for a density of $\alpha n_e(0)$ the signal enhancement given in the example of this section (e.g. Fig. 27c) is to be scaled by $\sim 10^{-(\alpha-1)}$. On the basis of this scaling it can be inferred that DNB doping beam measurements of the slowing-down spectra should be feasible for central electron densities up to $n_e(o) \sim 1.5 \times 10^{14}$ cm$^{-3}$.

## 8.0 BEAM-PLASMA EFFECTS

The requirement to provide active charge exchange diagnostics up to plasma densities of $n_e(o) \sim 2 \times 10^{14}$ cm$^{-3}$ leads to a diagnostic doping beam having appreciable power. For the horizontal and vertical CENA reference 80 keV diagnostic beams, the total neutral power for operation with hydrogen is ~440 kW and with deuterium is ~1060 kW. The latter corresponds to about 3% of the 4-beamline NBI heating power (33.5 MW deuterium at 120 keV full energy). At such power levels it is obviously necessary to examine the effect of the diagnostic beam on the plasma. In this section, perturbation of the

plasma temperature due to operation of the DNB doping beam is examined.

Two DNB operating scenarios were investigated: 1) a continuous mode consisting of a single pulse of 500 msec duration, and 2) a modulation mode consisting of a train of six pulses, each of 20 msec duration separated by 50 msec beam-off periods. The latter is the envisioned standard mode for DNB doping operation with a 50% duty cycle and beam pulse length from 10-50 msec.

The analysis utilizes the BALDUR one-dimensional transport code to compute the plasma response to the diagnostic neutral beam. Calculations were performed both for tangential orientation of the 80 keV-440 kW hydrogen beam and for perpendicular orientation of the 80 keV-1060 kW deuterium beam. The beam fired into an ohmically heated plasma ($T_e \sim T_i \sim 1.7$ keV) for line average electron densities ranging from $\bar{n}_e \cong 2\text{-}8 \times 10^{13}$ cm$^{-3}$. The code generated evolution of the ion temperature is shown in Fig. 30 for a tangential hydrogen DNB case. A continuous pulse of 500 msec duration is initiated 500 msec into the plasma discharge. This example is typical of the maximum ion temperature excursion since the line average density, $\bar{n}_e = 2 \times 10^{13}$ cm$^{-3}$, is low.

The DNB induced increment in the ion temperature is determined by comparing central ion temperatures with and without DNB operation. In Fig. 31, the fractional temperature increase, $\Delta T_i(o)/T_i(o)$, is plotted as a function of line average electron density for the horizontal-H° and perpendicular-D° reference doping beam parameters. The curves depict the continuous mode of operation and the data points at $\bar{n}_e = 4 \times 10^{13}$ cm$^{-3}$ show

show the effect of the modulation mode. All temperature increments are maximum values measured at the end of the beam pulse.

From the point of view of DNB doping measurements, the predicted ion temperature perturbation is, of course, undesirable. Provision to reduce this effect is made by incorporating two V-shaped calorimeters into the beamline which are adjustable in orthogonal directions to stop down the area of the beam cross section by a factor of 10 or more. With decreasing electron density, the amount by which the beam power must be stopped down increases. As can be seen from Fig. 22, even with the attendant loss in DNB doping signal enhancement, the viability of active temperature diagnostics for the perpendicular CENA system is not compromised. Since the signal levels are considerably higher for the fast ion measurements, this statement is valid for the horizontal CENA system as well.

## 9.0 ADVANCED APPLICATIONS

The emphasis of this report is on the use of the TFTR diagnostic beam to provide a source of doping neutrals for active charge exchange measurements. In addition to the basic measurement of the ion temperature radial profile and the slowing-down energy distribution of heating beam ions, DNB doping can be advantageously employed in a variety of what may be termed advanced charge exchange applications. Some examples that can be cited are:
1) spatial distribution of the plasma neutral density[13] including the source of neutral atoms arising due to NBI heating,[14]
2) plasma rotation induced by unbalanced co- and counter-injection

of neutral heating beams,[15] 3) ion cyclotron resonance heating effects including the spatial distribution[16] and isotropy[3] of majority/minority species ion energy spectra, and 4) effects of combined ion cyclotron and neutral injection heating.[17]

Another important aspect of a diagnostic beam capability is its use as an ion beam probe rather than a source of doping neutrals. Under certain experimental conditions, measurement of fast-ion orbit shifts (including beam molecular ion components[18]) has provided a means for directly measuring the safety factor, or q, profile in a tokamak.[19]

The charge exchange spectra near the injection energy of neutral beams[20] provides a plethera of information on topics such as: 1) classical slowing-down effects leading to, for example, radial measurement of $Z_{eff}$,[21] and 2) neoclassical effects on the orbits of injected beam ions.[14] In most cases, the above measurements were made viewing the energy distribution of the heating beam injected neutrals. For the TFTR charge exchange system, however, the appreciable power of the diagnostic beam makes it conceivable to view the slowing down spectra of the DNB particles either in place of or in addition to the NBI spectra. Use of the charge-exchange spectrum due to the DNB slowing-down energy distribution for diagnostic purposes merits further comment.

In Fig. 32, the NBDEN and BAFPS codes are used to simulate the DNB functioning simultaneously as a "heating beam" and a source of doping neutrals for its own slowing-down ion distribution. The "self-doped" charge exchange analyzer signal in the region of the 80 keV hydrogen neutral injection energy is shown in the upper

plot of Fig. 32. The ratio of the spectra with the self-doping (BEAM-ON) to that without DNB doping (BEAM-OFF) shown in the lower plot illustrates the large "self-enhancement" effect. During application of the DNB as a doping source, of course, the self-doped signal is always present. When convoluted with the slowing-down spectrum of the NBI heating beams, the resulting energy distribution could be difficult to interpret. This situation, however, is avoided by the design of the TFTR active charge exchange system. Specifically, by requiring capability for either hydrogen or deuterium DNB operation, one can choose a gas specie other than that being used for the NBI injection beams. Because of the mass resolving capability of the analyzers, the slowing-down energy distribution of the different DNB and NBI species are separable. In fact, both slowing-down distributions can be measured simultaneously under virtually all TFTR experimental conditions without significant interference with the target plasma thermal ion energy spectra measurements, thus offering a novel charge exchange diagnostic situation with interesting potential. Since the DNB is designed for operation at up to 80 keV using either hydrogen or deuterium species with beam aiming remotely adjustable over an angular range of 0 - 40° (see Fig. 3), it provides an extremely versatile ion beam probe. By suitable choice of the intersection of the beam axis and analyzer sightlines, radially resolved measurements of the self-doped DNB slowing-down spectra over a significant region of the plasma core is envisioned.

The plasma conditions used in obtaining the calculated spectra of Fig. 32 are characteristic of a full bore (a = 85 cm) ohmic

discharge with relatively low temperature ($T_e(o) = T_i(o) = 1$ keV) and high density ($n_e(o) = 8 \times 10^{13}$ cm$^{-3}$). Such a discharge is representative of the most difficult conditions envisioned for application of the DNB as an ion probe. This diagnostic method, therefore, can be anticipated to be viable over a wide range of TFTR ohmic heating conditions as well as in discharges having high temperatures due to auxiliary heating processes such as neutral beam injection, magnetic compression, and ion cyclotron resonance heating.

It is of interest to mention one further application of the DNB which exploits the perturbation of the ion temperature noted earlier when the DNB is operated at maximum power with relatively low plasma density ($n_e(o) \lesssim 5 \times 10^{13}$ cm$^{-3}$). In view of the design capability to vary the injection angle, it is conceivable that the DNB may be used to explore optimization of the heating beam injection angle by measuring the temperature perturbation using charge exchange and other diagnostics, for example, neutron measurements.

A detailed study of the advanced applications discussed briefly in this section will be presented in a future report.

## 10.0 SUMMARY

Enhancement of the charge exchange signal by use of a Diagnostic Neutral Beam (DNB) has been examined for the two Charge Exchange Neutral Analyzer (CENA) systems designed for the TFTR using code simulation of the neutral transport and charge exchange production processes. From the analysis results, it is concluded that a beam energy of 80 keV provides a reasonable

compromise between optimum doping efficacy and reliable ion source technology. For a 10 cm × 10 cm ion source extraction grid geometry, the total extracted ion current is nominally 15 A for deuterium operation and 17 A for hydrogen. At a fixed energy of 80 keV, signal enhancement is maximized by use of a deuterium beam for the vertical CENA system and a hydrogen beam for the horizontal CENA system. Active measurements of central ion temperatures in the range $T_i \geq 5$ keV for full bore plasma discharges (a = 85 cm) at central electron densities up to $n_e(o) \simeq 1.2 \times 10^{14}$ cm$^{-1}$ are feasible. At lower temperatures ($T_i \simeq 1$ keV), the density limit for DNB doping measurements decreases to $n_e(o) \sim 3 \times 10^{13}$ cm$^{-3}$. The density limit for active charge exchange measurement of the TFTR 120 keV heating beam slowing-down spectra using the horizontal CENA system is difficult to characterize because of the multiplicity of heating conditions including variation of injection angle with plasma density and use of magnetic compression heating. However, for tangential injection into a full bore (a = 85 cm) plasma, an upper density limit of $n_e(o) \simeq 1.5 \times 10^{14}$ cm$^{-3}$ is estimated which indicates that measurement of slowing-down spectra under magnetic compression scenarios should be feasible at the maximum TFTR operating density referenced at $n_e(o) = 2 \times 10^{14}$ cm$^{-3}$.

In addition to the charge exchange doping function, the diagnostic beam offers the potential for a broad range of diagnostic applications under use as a versatile ion beam probe.

ACKNOWLEDGEMENTS

The assistance of J. McEnerney and D. Miller in programming applications, A. L. Roquemore in analyzer model development, and C. Singer in BALDUR computations is gratefully acknowledged.

This report was supported by the Department of Energy under contract DE-AC02-76-CH03073.

## REFERENCES


1. C. R. Parsons and S. S. Medley, "On the Interpretation of Charge-Exchange Ion Temperature Measurements in Tokamaks," Plasma Physics 16, 267 (1974).
2. J. G. Cordey, "The Distortion of the Plasma Ion Distribution During Neutral Injection Heating," in Plasma Physics and Controlled Nuclear Fusion Research (Proceedings of the 5th International Conference, Tokyo, Japan, 1974) Vol. I, IAEA, Vienna, Austria (1975) p. 623-632. See also E. Bittoni, J. G. Cordey, and M. Cox, Nuclear Fusion (to be published).
3. J. Hosea, P. Colestock, S. Bernabei, S. L. Davis, P. Efthimion, R. J. Goldston, D. Hwang, S. S. Medley, D. Mueller, J. Strachan, and H. Thompson, "Fast Wave Heating of Two-Ion Plasmas in the Princeton Large Torus," Phys. Rev. Lett. 43, 1802 (1979).
4. D. E. Post, et al., "Status Report of TFTR Related Work by the PPL Theoretical Division Transport Code Group," PPPL Technical Memo TM-298 (1977).
5. C. E. Singer, "Updated 1-D Simulations of 2.5 MA TFTR D:T Discharges," TFTR Physics Group Report #22 (1980).
6. H. H. Towner, "A 3-Dimensional Neutral Transport Code: NBDEN," PPPL Report (in preparation).
7. Developed by R. J. Goldston, Princeton PPL.
8. R. J. Goldston, "A Simple Neutral Density Profile Calculation for Tokamaks with $\lambda_{mfp} << a$," Plasma Phys. 20, 1199 (1978).
9. R. Kaita and S. S. Medley, "A Study of the Mass and Energy Resolution of the E||B Charge Exchange Analyzer for TFTR," PPL-1582 (1979).

10. S. L. Davis, S. S. Medley and M. Brusati, "The Charge Exchange Analyzer for Mass Resolved Ion Temperature Measurements on PLT," PPPL-1478 (1978).

11. S. S. Medley, "Vacuum System Design and Tritium Inventory for the TFTR Charge Fxchange Diagnostic," PPPL-1551 (1979).

12. H. H. Towner and R. J. Goldston, "NBDEN - A 3-D Code to Study $n_o(r, \theta, \phi)$ Due to Neutral Injection," Bull. Am. Phys. Soc. 24, 1107 (1979).

13. M. Brusati, "A Proposal for Measuring the Local Ion Distribution Function and the Neutral Density Profile in Toroidal Plasmas," Nucl. Fus. 17, 144 (1977).

14. R. Kaita and R. J. Goldston, "Recent Results of PLT Fast Ion Diagnostic Experiments," Bull. Am. Phys. Soc. 24, 1107 (1979).

15. H. Eubank, et al., "PLT Neutral Beam Heating Results," in Plasma Physics and Controlled Nuclear Fusion Research (Proc. 7th International Conference, Innsbruck, Austria, 1978) Vol. I, IAEA, Vienna, 1979, p. 167-197.

16. J. Hosea, et al., "Fast Wave Heating in the Princeton Large Torus," PPPL-1588 (1979).

17. S. S. Medley, et al., "Charge Exchange Measurements During Neutral Beam Injection and ICRF Heating on PLT," in Controlled Fusion and Plasma Physics (Proc. 9th European Conf., Oxford, England, 1979) Vol. I, Culham Laboratory, 1979, p. 49.

18. K. H. Berkner, R. V. Pyle, and J. W. Stearns, "Intense, Mixed-Energy Hydrogen Beams on CTR Injection," Nucl. Fus. 15, 249 (1975).

19. R. J. Goldston, "Radially Resolved Measurements of "q" on the Adiabatic Toroidal Compressor Tokamak," Phys. Fluids 21, 2346 (1978).

20. R. J. Goldston "Charge-Exchange Spectra Near the Injection Energy in Tokamaks Equipped with Tangential Neutral Beams," Nucl. Fusion 15, 651 (1975).

21. R. J. Goldston, "Fast Ion Experiment on ATC: Radially Resolved Measurements of q, $Z_{eff}$, $T_{i\parallel}$ and $T_{i\perp}$," Ph.D. Thesis, Princeton University, PPL-1432 (1977).

22. J. W. Stearns, K. H. Berkner, and R. V. Pyle, "Neutral-Beam Design Options," LBL-4492 (1976).

23. A. C. Riviere, "Penetration of Fast Hydrogen Atoms into a Fusion Reactor Plasma" Nucl. Fus. 11, 363 (1971).

24. R. L. Freeman and E. M. Jones, "Atomic Collision Processes in Plasma Physics Experiments," CLM-R 137 (1974).

25. R. E. Olson, et al., "Charge-State Dependence of Electron Loss from H by Collisions with Heavy, Highly Stripped Ions," Phys. Rev. Lett. 41, 163 (1978).

## APPENDIX A

The following is an account of the diagnostic beam parameters used to evaluate the charge exchange neutral doping performance as a function beam energy. The LBL Mark III prototype ion source is used as the model for the TFTR diagnostic beam. Since specifications for this source are not available over the desired range of extraction energy, the total full-energy-equivalent extracted ion current, $I_T^+(A)$ is scaled according to

$$I_T^+(A) = \alpha\ V^{3/2}\ (kV) \qquad (A\text{-}1)$$

where V (kV) is the extraction voltage. The constant, $\alpha$, is determined from the known MARK III performance data shown in Table A-I. Thus for hydrogen

$$I_{TH}^+ = 0.024\ V^{3/2} \qquad (A\text{-}2)$$

and for deuterium

$$I_{TD}^+ = 0.021\ V^{3/2} \qquad (A\text{-}3)$$

The total extracted ion current is comprised mainly of mono-, di-, and tri-atomic ions at the full extraction energy, for example, $H_1^+(E)$, $H_2^+(E)$, and $H_3^+(E)$. Conventionally, the current fractions carried by these components are quoted as one of the source specifications. For example, if the total current is $I_T^+ \approx 17$ A and the full energy current fractions $a_1$, $a_2$, and $a_3$ have the values given in Table A-I, then the currents $I_m^+ = a_n I_T^+$ carried

by the respective molecular species are 11.9 A, 4.25 A, and 0.85 A. In the neutralizer, the molecular ions split into atomic species at energies E, E/2, and E/3. Since the power, $P_m = EI_m^+$ in each molecular component cannot change in the neutralizer, the current carried by the atomic energy components becomes $I_n^+ = nI_m^+$. Continuing the above example, the currents carried by the atomic species at the full, one-half, and one-third extraction energies are respectively 11.9 A, 8.50 A, and 2.55 A. The atomic currents are thus given by:

$$I_n^+ = n\, a_n\, I_T^+ \tag{A-4}$$

and the atomic current fractions by:

$$b_n = \frac{na_n}{\Sigma\, na_n} \tag{A-5}$$

where the energy components are $E_n = E/n$. Although the full energy current fractions, $a_n$, are known to depend weakly on the extraction energy, no information on this is available at present for the source model. Hence the values appropriate for 80 kV-H listed in Table A-I will be used at all energies for both hydrogen and deuterium. The atomic ion current components are neutralized in a near-equilibrium neutralizer,[22] for which some typical efficiencies, $\eta(E)$, are shown in Table A-II. Thus the desired atomic neutral energy currents are given by:

$$I_n^{\circ} = \eta(E_n)\, n\, a_n\, I_T^+ \quad . \tag{A-6}$$

The parameters used in this study for the diagnostic neutral beam currents as a function of extraction energy follow directly from the above deliberations. In Table A-III, the total ion currents at extraction energies of 20, 40, 60, 80, and 100 keV are given using Eq. A-2 for hydrogen and Eq. A-3 for deuterium. The full, half, and third energy neutral current fractions follow from Eq. A-6. The results are plotted in Fig. 6.

TABLE A-I

CHARACTERISTICS OF THE
MODEL ION SOURCE

| | |
|---|---|
| Full Energy (E) | 80 keV |
| Total Current ($I_T$) | 17 A (Hydrogen)<br>15 A (Deuterium) |
| Current Fractions: | $a_1 = 0.70 - H_1^+(E)$<br>$a_2 = 0.25 - H_2^+(E)$<br>$a_3 = 0.05 - H_3^+(E)$ |
| Divergence: | |
| Parallel to slots: | 0.4° |
| Perpendicular to slots: | 1.2° |
| Grids: Dimensions: | 10 cm × 10 cm |
| Focussing: | ∞ |

TABLE A-II

NEUTRALIZER PARAMETERS

| Ion Energy (keV) | Neutralization Fraction, $\eta$ | |
|---|---|---|
| | Hydrogen | Deuterium |
| 20 | 0.80 | 0.90 |
| 40 | 0.54 | 0.80 |
| 60 | 0.38 | 0.66 |
| 80 | 0.22 | 0.54 |
| 100 | 0.12 | 0.46 |

TABLE A-III

DIAGNOSTIC BEAM NEUTRAL CURRENTS

| SPECIES | V(kV) | $I_m^+$(A) | $I_1$(A) $H_1^\circ$(E) | $I_2$(A) $H_1^\circ$(E/2) | $I_3$(A) $H_1^\circ$(E/3) |
|---|---|---|---|---|---|
| Hydrogen | 20 | 2.2 | 1.20 | 0.99 | 0.30 |
| | 40 | 6.1 | 2.31 | 2.38 | 0.83 |
| | 60 | 11.2 | 2.98 | 3.56 | 1.31 |
| | 80 | 17.0 | 2.62 | 4.59 | 1.66 |
| | 100 | 24.0 | 2.02 | 5.52 | 2.16 |
| Deuterium | 20 | 1.9 | 1.20 | 0.80 | 0.26 |
| | 40 | 5.3 | 2.99 | 2.38 | 0.75 |
| | 60 | 9.8 | 4.52 | 4.16 | 1.32 |
| | 80 | 15.0 | 5.67 | 6.00 | 1.91 |
| | 100 | 21.0 | 6.76 | 7.67 | 2.68 |

## APPENDIX B

The codes used for the analysis presented in this report require input of various TFTR machine and plasma parameters. In most cases, the analysis results are not sensitive to these parameters.

The values given below are presented in the interest of defining a "reference parameter set."

### B-1. Plasma/Discharge Parameters

| | |
|---|---|
| Major radius ($R_o$) | 248 cm |
| Minor radius (a) | 85 cm |
| Plasma current ($I_p$) | 2.5 MA |
| Toroidal field ($B_\phi$) | 5.2 Tesla @ $R_o$ |
| q (on axis) | 1.0 |
| Loop voltage | 1.5 Volts |
| Plasma ion mass | 2.0 |
| Impurity ion mass | 30.0 |
| Impurity ion charge | 12.0 |
| $Z_{eff}$ | 2.0 |
| Neutral edge density | $3.5 \times 10^8$ $cm^{-3}$ |
| Neutral edge temperature | 35 eV |

### B-2. Neutral Beam Injection (NBI) Heating Parameters

| | |
|---|---|
| Beam atomic mass | 2.0 |
| Injection voltage | 120 keV |
| Injection power | 33.5 MW |

B-2. Neutral Beam Injection (NBI) Heating Parameters (Continued)

| | |
|---|---|
| Current fractions | E : 0.42 |
| | E/2: 0.33 |
| | E/3: 0.25 |
| Major radius of beam tangency | 230 cm |

## APPENDIX C

The total attenuation cross section, $\sigma_T$, used in the neutral transport and Fokker-Planck codes to calculate the attenuation of the neutral particles is obtained from empirical fits to the cross sections for charge exchange ($\sigma_{cx}$), and impact ionization on electrons ($\sigma_{ie}$), protons ($\sigma_{ip}$), and impurity ions. The fitting equations used are presented here. All cross sections are in units of $cm^2$.

The cross section for charge exchange of protons on hydrogen atoms is given by:[23]

$$\sigma_{cx} = \frac{0.6937 \times 10^{-14} \left(1 - 0.155 \log \frac{E}{M}\right)^2}{1 + 0.1112 \times 10^{-14} \left(\frac{E}{M}\right)^{3.3}} \qquad \text{(C-1)}$$

where M is the proton or deuteron mass in AMU and E is the particle energy in electron volts.

The electron impact ionization cross section[24] is given by

$$\sigma_{ie} = \frac{\langle \sigma v \rangle}{V_o} = \frac{e^{\chi_{ie}}}{V_o}$$

where

$$\chi_{ie} \approx \sum_{i=o}^{6} A_i (\ln T_e)^i \qquad \text{(C-2)}$$

and

$$A_o = -0.2294140 \times 10^2$$

$$A_1 = 0.3209821 \times 10^1$$

$$A_2 = -0.7180771$$

$$A_3 = 0.9188585 \times 10^{-1}$$

$$A_4 = -0.8202399 \times 10^{-2}$$

$$A_5 = 0.4398966 \times 10^{-3}$$

$$A_6 = 0.1002732 \times 10^{-4} \quad .$$

The electron temperature, $T_e$, is in units of electron volts and the neutral velocity, $V_o$, in cm/sec is

$$V_o = 1.384 \times 10^6 \sqrt{\frac{E_o}{A}}$$

where $E_o$ is the neutral energy in eV and A is the atomic mass in AMU.

The proton impact ionization cross section[24] is given in $\sigma_{ip} = e^{\chi_{ip}}$ where

$$\chi_{ip} = \sum_{i=o}^{6} A_i (\ln \frac{E}{A})^i \qquad \text{(C-3)}$$

and

$$A_o = -0.4203309 \times 10^2$$

$$A_1 = 0.3557321 \times 10^1$$

$$A_2 = -0.1045134 \times 10^1$$

$$A_3 = 0.3139238$$

$$A_4 = -0.7454475 \times 10^{-1}$$

$$A_5 = 0.8459113 \times 10^{-2}$$

$$A_6 = -0.3495444 \times 10^{-3} \quad .$$

Here E is the relative energy between the proton and the neutral in keV and A is the mass of the neutral in AMU.

The cross section for electron loss from neutral hydrogen isotopes due to charge exchange and impact ionization on impurity ions is given by[25]

$$\sigma_I = 4.6\ q \times 10^{-16}\ (32\ \frac{q}{E}) \left[1 - \exp(-\frac{E}{32q})\right] \qquad \text{(C-4)}$$

where q is the ion charge state, and E is the relative energy between the neutral and impurity ion in keV/AMU.

The plasma ion depletion (ratio of proton to electron density) is

$$\frac{n^+}{n_e} = \frac{Z_I - Z_{eff}}{Z_I - 1} \qquad \text{(C-5)}$$

and the impurity ion density fraction is

$$\frac{n_I}{n_e} = \frac{Z_{eff} - 1}{Z_I - 1} \cdot \frac{1}{Z_I} \quad . \qquad \text{(C-6)}$$

Here $Z_{eff}$ is the effective plasma Z and $Z_I$ is the charge state of the designated dominant impurity species. Dilution effects of the heating beam ions are not included.

Combining the above relations gives the total cross section expression

$$\sigma_T = \frac{n^+}{n_e} (\sigma_{cx} + \sigma_{ip}) + \frac{n_I}{n_e} \sigma_I + \sigma_{ie} \quad . \qquad \text{(C-7)}$$

## APPENDIX D

Specifications of some of the salient parameters for the TFTR prototype E||B charge exchange analyzer are given below. Included are aspects of the microchannel plate detector and the vacuum interface between the analyzer and the torus.

| | |
|---|---|
| **Stripping Cell** | |
| Length | 20 cm |
| Aperture diameter | |
| Entrance | 0.3 cm |
| Exit | 0.4 cm |
| Pressure (He) | 10 mTorr |
| **Analyzer** | |
| Magnet pole radius | 20 cm |
| Pole separation | 6.0 cm |
| Electrode separation | 5.8 cm |
| Magnetic field (max.) | 5.5 kG |
| Electric field (max.) | 1.0 kV/cm |
| **Detector** | |
| Length of active area (Y) | 38 cm |
| Width of active area | 1 cm |
| Number of active columns | 3 |
| Separation of active columns (center-to-center) | 1.5 cm |
| Number of anode pads per column | 75 |
| Width of anode pads ($\Delta$Y) | 0.4 cm |

Vacuum Interface

| | |
|---|---|
| Length of flight tube (from midpoint of stripping cell to vacuum vessel port) | |
| Vertical CENA system | 720 cm |
| Horizontal CENA system | 485 cm |
| Effective aperture diameter of flight tube (at the vacuum vessel port) | |
| Vertical CENA system | 2.86 cm |
| Horizontal CENA system | 5.00 cm |

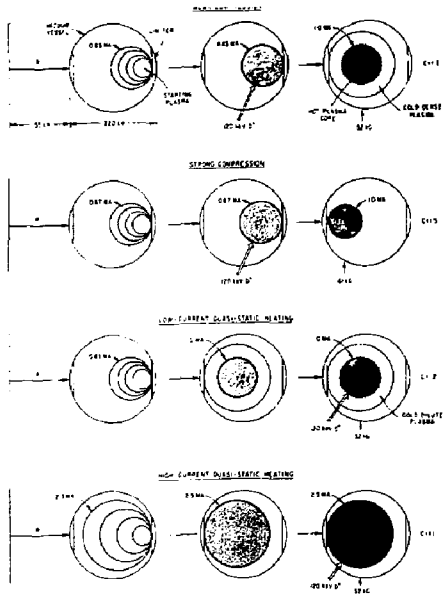

(PPPL-753877)
Fig. 1. Four representative modes of experimental operation in the TFTR device.

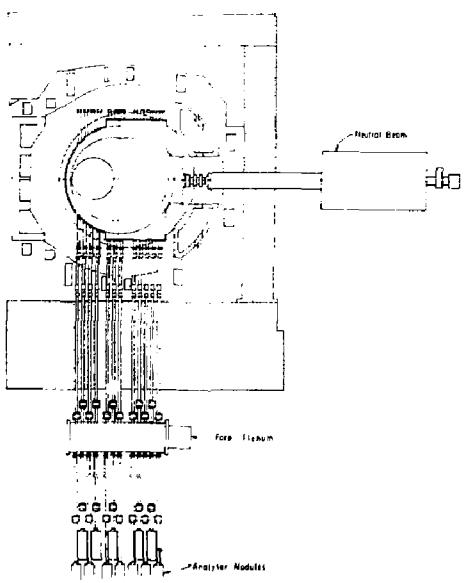


(PPPL-793441)
Fig. 2. Schematic of the vertical Charge Exchange Neutral Analyzer (CENA) system. The arrangement of the twelve analyzer modules and the Diagnostic Neutral Beam (DNB) are shown.

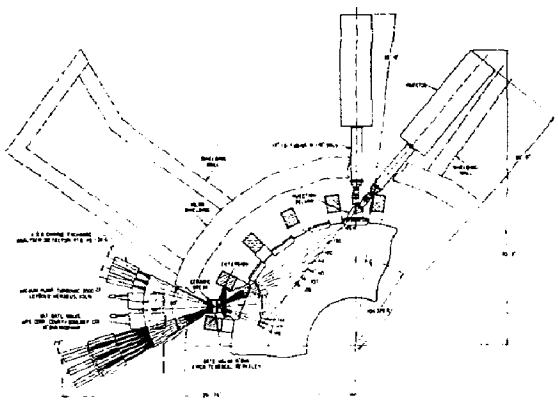

(PPPL-783808)
Fig. 3. Sectional top view of the TFTR torus showing the layout of the horizontal Charge Exchange Neutral Analyzer (CENA) system and the extreme perpendicular and tangential positions for the continuously steerable diagnostic neutral beam.

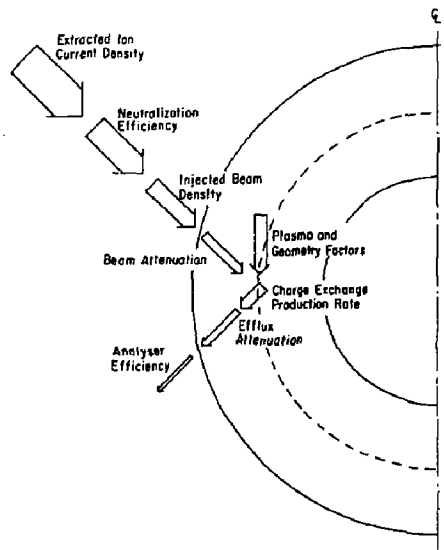


(PPPL-783982)
Fig. 4. Flow schematic illustrating the analysis steps used in evaluation of the DNB performance.

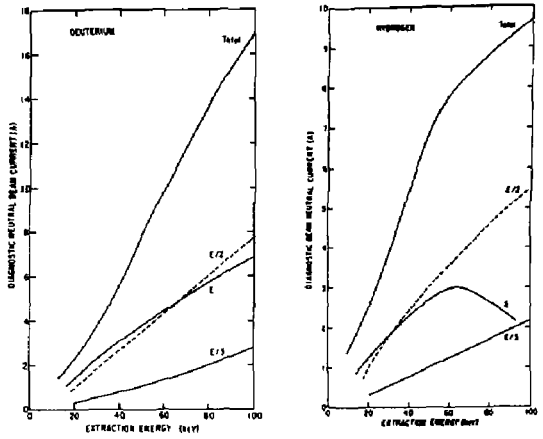


(PPPL-803483)
Fig. 5. Deuterium and hydrogen neutral beam currents as a function of ion source extraction energy used for the DNB model. The total current is comprised of full (E), half (E/2), and third (E/3) energy components.

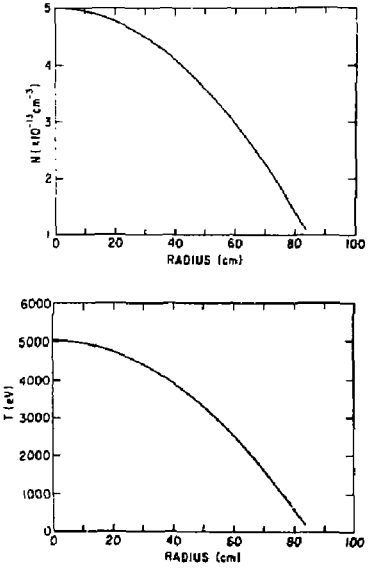


(PPPL-803485)
Fig. 6. Reference TFTR radial profiles for the electron density, N, and plasma ion/electron temperature, T, provided by BALDUR one-dimensional transport code calculations.

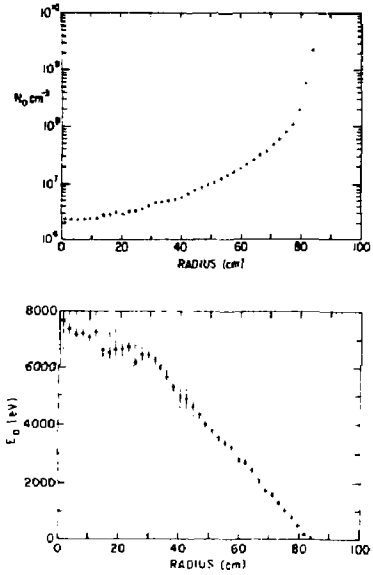


(PPPL-803484)

Fig. 7. Radial profiles of the wall neutral density, $N_o$, and the mean neutral energy, $E_o$, generated by the BALDUR code under the same plasma simulation conditions as used to obtain the profiles shown in Fig. 6.

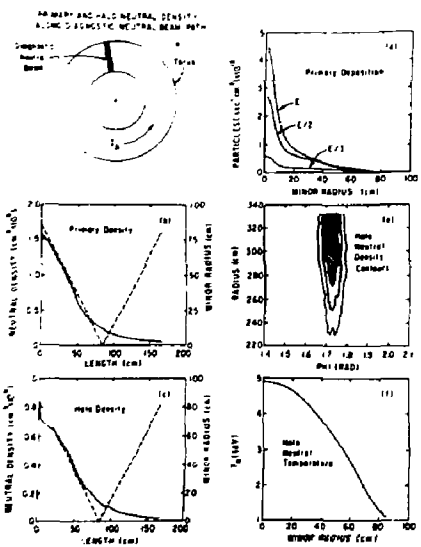

(PPPL-803591)

Fig. 8. Illustration of the NBDEN neutral transport code calculations for the case of 80 keV deuterium DNB doping in the viewing field of the vertical CENA system. The plots show: (a) orientation of the DNB to intersect the sightlines of the vertical CENA system located beneath the torus, (b) DNB primary neutral density as a function of beam penetration path length, (c) halo neutral density as a function of path length, (d) deposition of DNB primary particles as a function of minor radius, (e) contours of the halo neutral density in the torus midplane as a function of major radius and toroidal angle phi, and (f) radial profile of the halo neutral temperature.

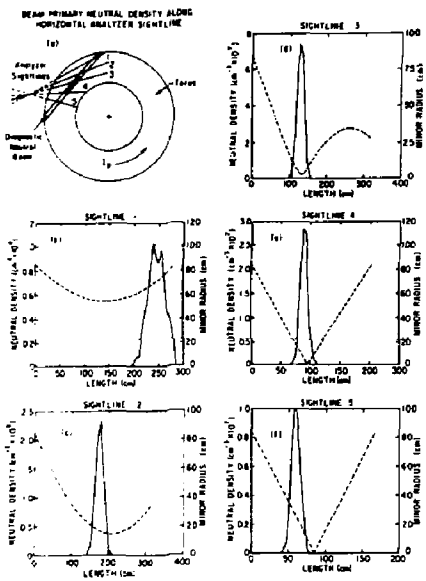

(PPPL-803590)

Fig. 9. Illustration of the NBDEN neutral transport code calculations for the case of 80 keV hydrogen DNB doping in the viewing field of the horizontal CENA system . The plots show: (a) orientation of the DNB and the designated analyzer sightlines 1-5 in the midplane of the torus, and (b)-(f) the primary neutral density as a function of position along each of the five analyzer sightlines. The dashed lines give the minor radius associated with position along the analyzer sightline.

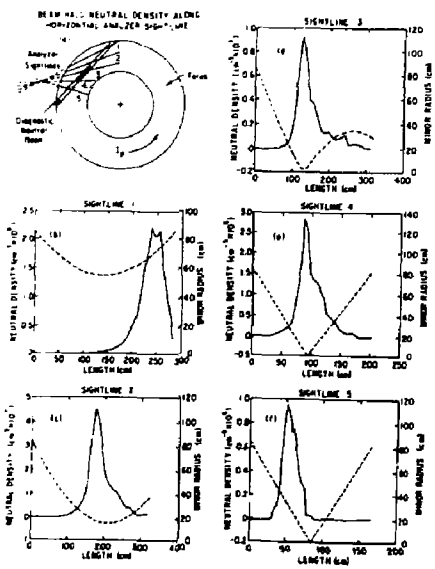

(PPPL-803592)

Fig. 10. Halo neutral density distributions as a function of sightline position for the same conditions as Fig. 9.

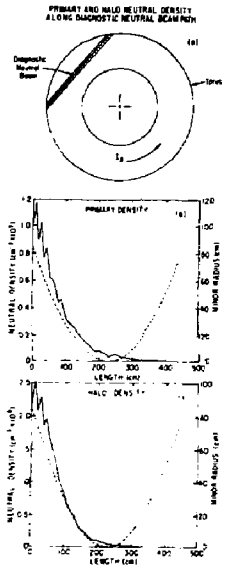

(PPPL-803593)

Fig. 11. Density of the primary and halo neutrals as a function of beam penetration length corresponding to the 80 keV hydrogen DNB case shown in Figs. 9 and 10.

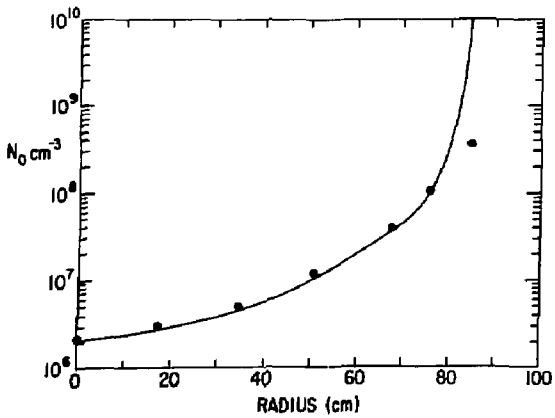


(PPPL-803580)

Fig. 12. Comparison of the wall neutral radial profile generated by the Monte Carlo method in the BALDUR code (solid line) with the simplified neutral calculation (data points) of the bounce-averaged Fokker-Planck code, BAFPS, used to simulate the charge exchange spectra.

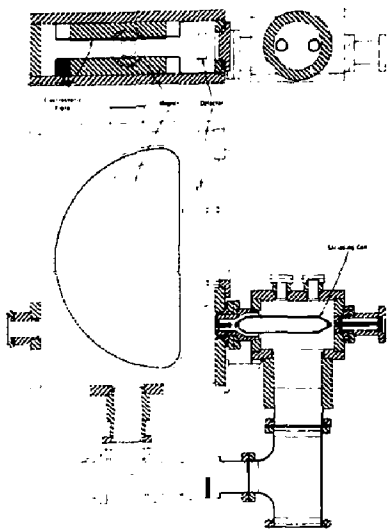

(PPPL-803271)
Fig. 13. Schematic of the prototype E||B Charge Exchange Neutral Analyzer (CENA) showing the major components discussed in the instrumental response model. Scale is approximately 1/8 full size.

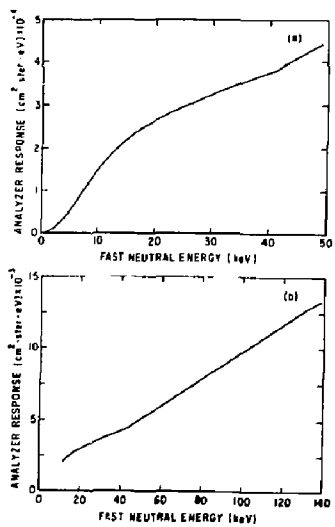


(PPPL-803355)
Fig. 14. Instrumental response curves for the vertical (A) and horizontal (B) CENA analyzer models.

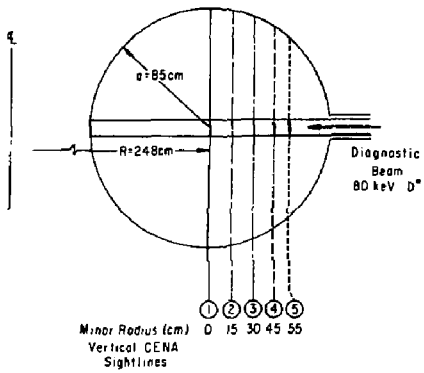


(PPPL-803308)

Fig. 15. Configuration of the analyzer sightlines used in the analysis of the DNB doping performance for the vertical CENA system. In the figures displaying analysis results associated with this section, the curves are identified with the analyzer sightlines by keying the line-style (solid, dashed, etc.) according to the legend shown in this figure.

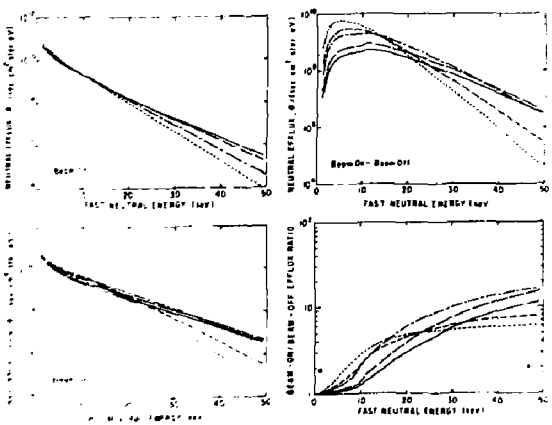

(PPPL-803594)

Fig. 16. Charge exchange neutral efflux as a function of energy for the vertical CENA sightlines shown in Fig. 15. Shown is the efflux without DNB doping (BEAM OFF), with 80 keV-D° DNB doping (BEAM ON), the efflux due to charge exchange on only doping neutrals given by the difference of these spectra (BEAM ON - BEAM OFF), and the ratio BEAN ON/BEAM OFF of the spectra with and without DNB doping.

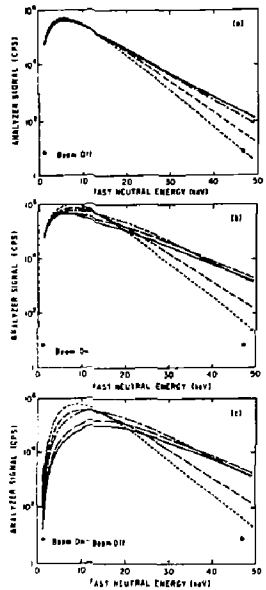


(PPPL-803311)

Fig. 17. Detected signal count rate as a function of fast neutral energy obtained by applying the analyzer response function (Fig. 14A) to the associated efflux spectra of Fig. 16. The asterisks denote the lower and upper energy limits of the detector at an analyzer magnetic field of B =2.0 kGauss.

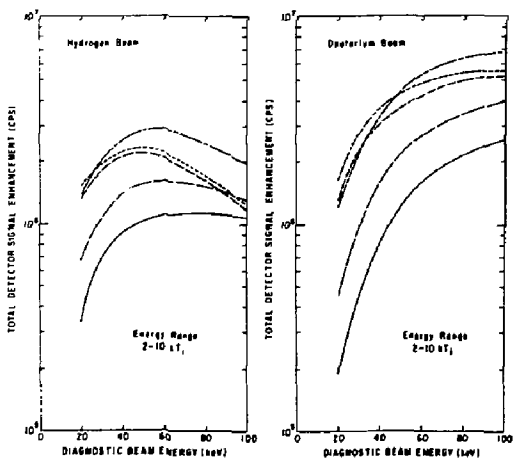


(PPPL-803234)

Fig. 18. Vertical CENA signal enhancement (see text) as a function of ion source extraction energy for hydrogen and deuterium neutral doping beams. Plasma parameters: $T_e(0) = T_i(0) = 5$ keV and $n_e(0) = 5 \times 10^{13}$ cm $^{-3}$ (reference data set).

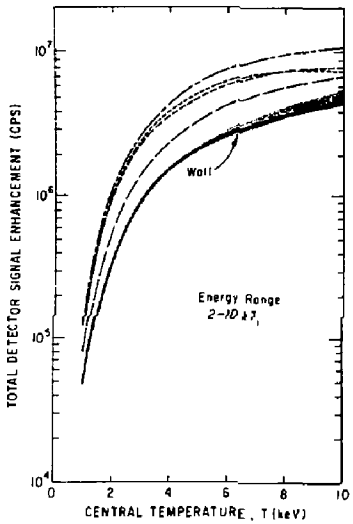


(PPPL-803235)
Fig. 19. Variation of vertical CENA signal enhancement with plasma temperature ($T_e = T_i$) for fixed electron density, $n_e(0) = 5 \times 10^{13}$ $cm^{-3}$ and an 80 keV deuterium doping beam.

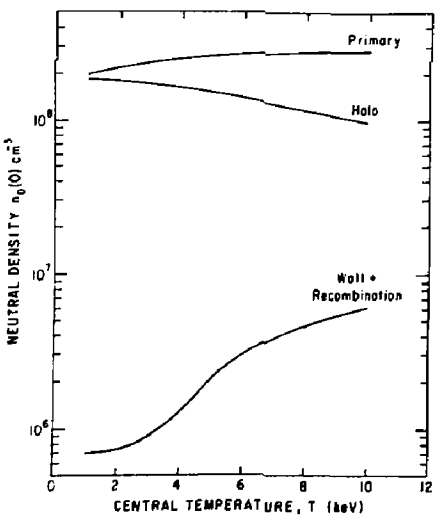


(PPPL-803584)
Fig. 20. Central density of the wall and doping beam neutrals as a function of plasma temperature for the conditions noted in Fig. 19.

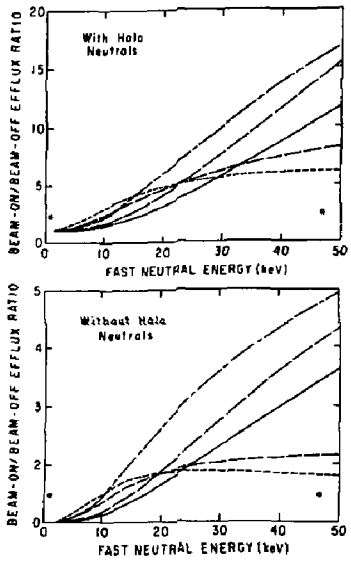


(PPPL-803585)

Fig. 21. Illustration of the contribution of the halo doping neutrals to the vertical CENA signal enhancement (80 keV deuterium DNB and reference plasma parameters). The top plot shows beam-on/beam-off efflux ratio due to charge exchange on both primary and halo doping neutrals while the bottom plot shows the effect of just the primary neutrals.

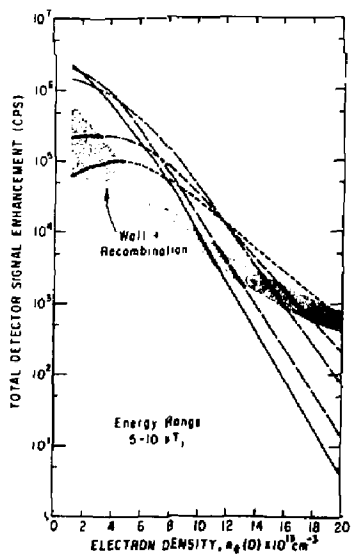


(PPPL-803306)

Fig. 22. Variation of the vertical CENA signal enhancement with scaling of the electron density (see text) for fixed plasma temperature, $T_e(0) = T_i(0) = 5$ keV. Note that in this case the signal enhancement is determined for charge exchange neutral energies in the range 5-10 $kT_i$. The shaded region shows the corresponding count rate due to charge exchange on the wall neutrals only, the spread reflecting the signal range over the five analyzer sightlines.

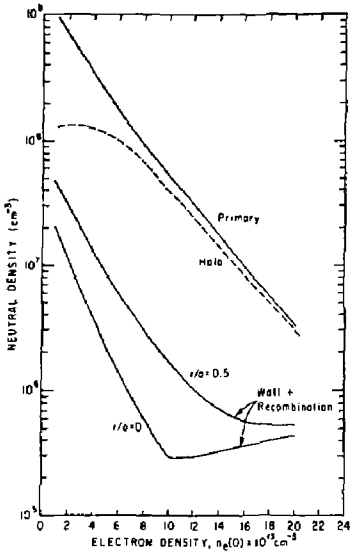


(PPPL-803336)
Fig. 23. Central density of the wall and doping beam neutrals with scaling of the plasma electron density as noted in Fig. 22.

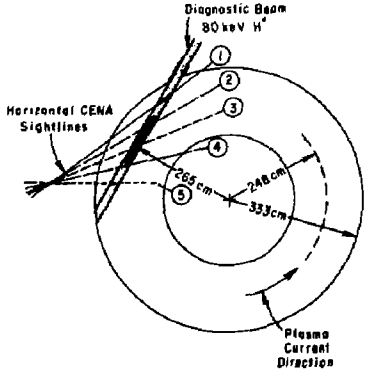


(PPPL-803335)
Fig. 24. Configuration of the analyzer sightlines used in the analysis of the DNB doping performance for the horizontal CENA system. The analyzer sightlines and the analysis results are key with the same line-style (solid, dashed, etc.) according to the legend shown in this figure.

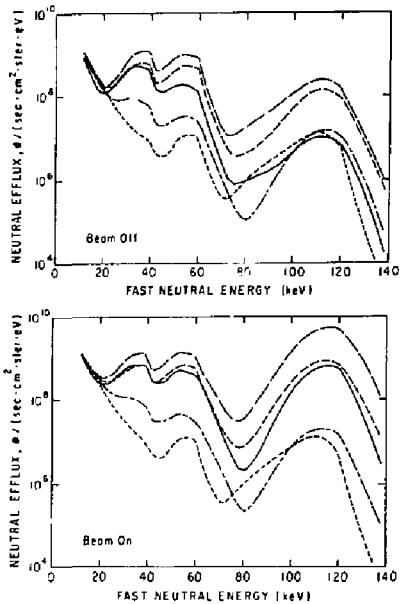


(PPPL-803637)

Fig. 25. Charge exchange neutral efflux spectra for the horizontal CENA sightlines designated in Fig. 24. The spectra exhibit the full, half, and third energy peaks corresponding to the slowing-down distribution of 120 keV deuterium NBI heating. The top plot shows the neutral efflux without the doping beam (BEAM OFF) while the bottom plot is with the 80 keV hydrogen doping beam (BEAM ON).

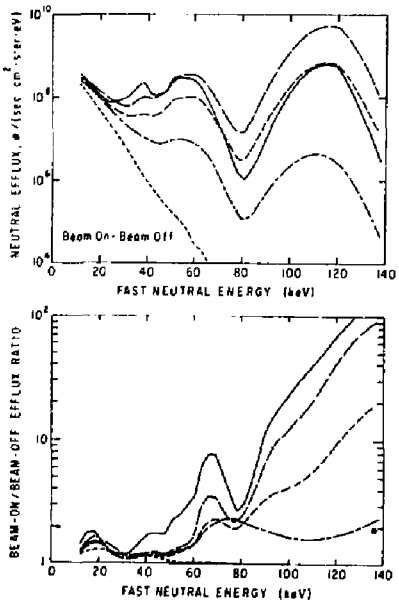


(PPPL-803636)

Fig. 26. The efflux due to charge exchange only on doping neutrals is displayed in the top plot by taking the difference (BEAM ON - BEAM OFF) of the spectra given in Fig. 25. The bottom plot shows the ratio of the spectra.

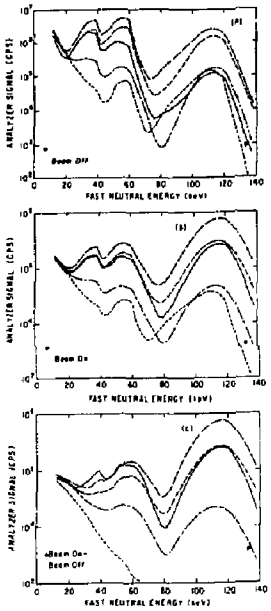


(PPPL-803310)

Fig. 27. Horizontal CENA detector count rate as a function of fast neutral energy obtained by applying the analyzer response function (Fig. 14B) to the efflux spectra shown in Fig. 25 and 26. The asterisks denote the lower and upper energy limits for the analyzer operated at a magnetic field of B = 3.4 kGauss.

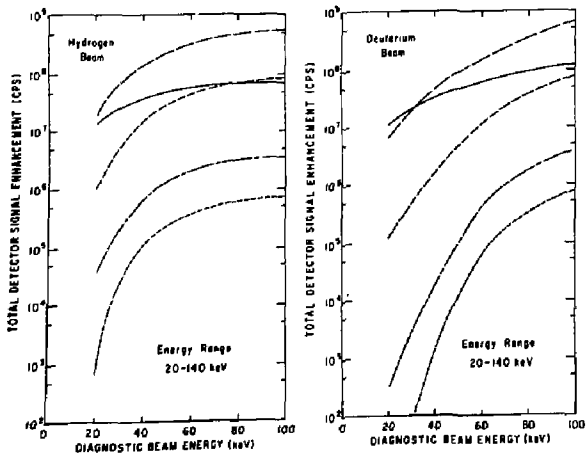


(PPPL-803305)

Fig. 28. Detector signal enhancement in the neutral efflux energy range 20-140 keV (see text) as a function of ion source extraction energy for hydrogen and deuterium doping beams. Plasma parameters: $T_e(0) = T_i(0) = 5$ keV and $n_e(0) = 5 \times 10^{13}$ cm$^{-3}$ (reference data set). Curves are keyed to the analyzer sightlines by the line-style (see Fig. 24).

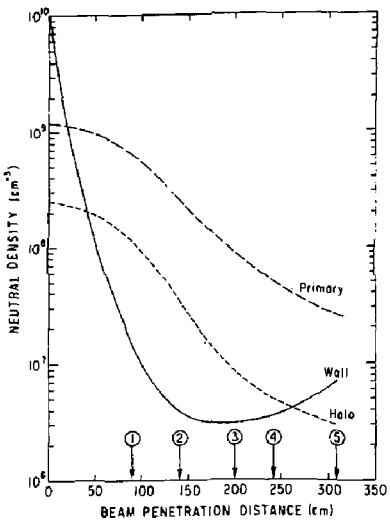


(PPPL-803309)

Fig. 29. Density of the wall and doping beam neutrals as a function of distance along the beam axis. Intersection points with the five analyzer sightlines are flagged.

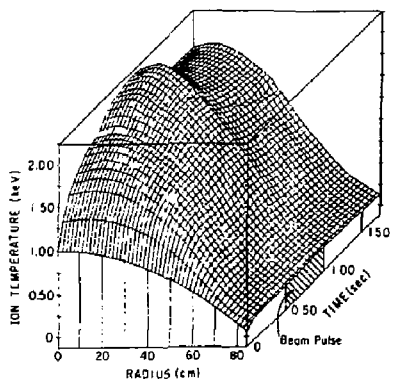


(PPPL-803702)

Fig. 30. BALDUR generated evolution of the ion temperature for tangential injection of the 80 keV-440 kW hydrogen diagnostic neutral beam into an ohmic TFTR plasma ($T_e \sim T_i \sim 1$ keV) at a line average electron density of $\bar{n}_e = 2 \times 10^{13}$ cm$^{-3}$.

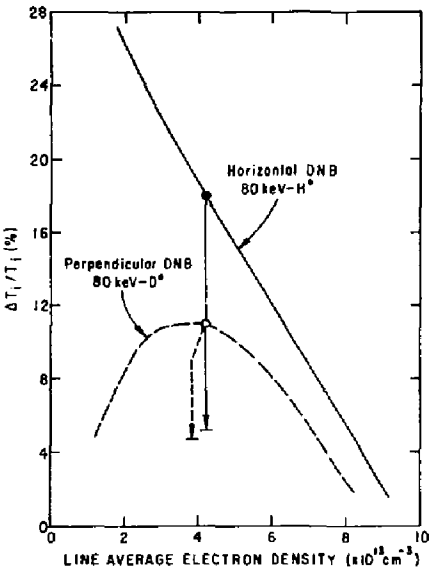


(PPPL-803589)

Fig. 31. Ion temperature fractional increase due to full power DNB operation as a function of line average electron density in ohmically heated TFTR discharges (a = 85 cm).

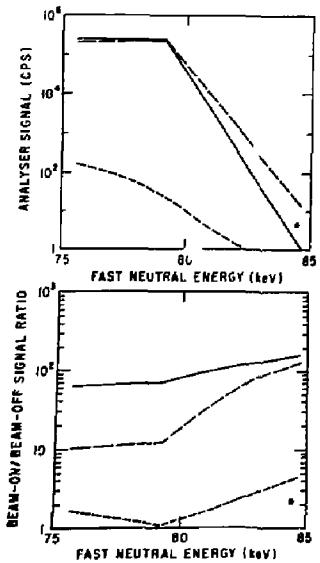


(PPPL-803587)

Fig. 32. Horizontal CENA signal viewing the self-doped slowing-down distribution of the tangential hydrogen DNB in the region of the beam energy, 80 keV (top). Plasma conditions: $T_e(0) = T_i(0) = 1$ keV, $n_e(0) = 8 \times 10^{13}$ cm$^{-3}$, and a = 85 cm. The bottom plot shows the signal enhancement ratio due to doping of the DNB ion spectra on its own neutral distribution. In both plots the linestyle is keyed to the analyzer sightline as shown in Fig. 24.